Title

Energy Metabolism Dysregulation in Chronic Kidney Disease.

Journal

Kidney360, 4(8)

Authors

Li, Ying

Gu, Wanjun

Hepokoski, Mark

et al.

Publication Date

2023-08-01

DOI

10.34067/KID.0000000000000153

Peer reviewed

Original Investigation

Kidney360

Energy Metabolism Dysregulation in Chronic Kidney Disease

Ying Li,[1,2] Wanjun Gu,[3] Mark Hepokoski,[2,3] Hai Pham,[1,2] Rick Tham,[1,2] Young Chul Kim,[1,2] Tatum S. Simonson,[3] and Prabhleen Singh[1,2]

Key Points

- There is significant enrichment in metabolic pathways in early stages in the subtotal nephrectomy model of CKD.
- Proximal tubular mitochondrial respiration is suppressed likely from mitochondrial dysfunction in substrate utilization and ATP synthesis.
- There is significant suppression of pyruvate dehydrogenase and increased glycolysis in proximal tubules.

Abstract

Background CKD is a significant contributor to morbidity and mortality. A better understanding of mechanisms underlying CKD progression is indispensable for developing effective therapies. Toward this goal, we addressed specific gaps in knowledge regarding tubular metabolism in the pathogenesis of CKD using the subtotal nephrectomy (STN) model in mice.

Methods Weight- and age-matched male 129X1/SvJ mice underwent sham or STN surgeries. We conducted serial GFR and hemodynamic measurements up to 16 weeks after sham and STN surgery and established the 4-week time point for subsequent studies.

Results For a comprehensive assessment of renal metabolism, we conducted transcriptomic analyses, which showed significant enrichment of pathways involved in fatty acid metabolism, gluconeogenesis, glycolysis, and mitochondrial metabolism in STN kidneys. Expression of rate-limiting fatty acid oxidation and glycolytic enzymes was increased in STN kidneys, and proximal tubules in STN kidneys exhibited increased functional glycolysis but decreased mitochondrial respiration, despite an increase in mitochondrial biogenesis. Assessment of the pyruvate dehydrogenase complex pathway showed significant suppression of pyruvate dehydrogenase, suggesting decreased provision of acetyl CoA from pyruvate for the citric acid cycle to fuel mitochondrial respiration.

Conclusion Metabolic pathways are significantly altered in response to kidney injury and may play an important role in the disease progression.

KIDNEY360 4: 1080–1094, 2023. doi: https://doi.org/10.34067/KID.0000000000000153

Introduction

CKD is an important public health problem with high risk of morbidity and mortality. CKD affects more than 25 million people in the United States, accounting for 15% of the total population.[1] With limited treatment options, patients with CKD progress to end stage kidney disease with an average survival of 3–5 years, which is worse than most cancers. Tubulointerstitial fibrosis (TIF), rather than glomerular injury, determines the clinical prognosis in CKD. A primary role of the proximal tubule in the initiation of TIF after injury has been established.[2,3] Investigating and targeting the initial tubular events have the potential to identify efficient therapeutic strategies to halt the downstream pathways that eventually lead to TIF.

Renal energy metabolism is central to cellular health and function because of the high metabolic demands of the kidney. The kidney exhibits a high rate of oxygen consumption to support the energy requirements of tubular reabsorption of filtered solutes. Most of the energy to support solute reabsorption in the kidney is derived from mitochondrial oxidative phosphorylation (OXPHOS) in renal tubules.[4] The proximal tubule segment in the cortex and thick ascending limb in the

[1]Division of Nephrology and Hypertension, University of California San Diego, San Diego, California
[2]VA San Diego Healthcare System, San Diego, California
[3]Division of Pulmonary, Critical Care and Sleep Medicine, University of California San Diego, San Diego, California

Correspondence: Dr. Prabhleen Singh, Division of Nephrology-Hypertension, University of California San Diego and VA San Diego Healthcare System, 3350 La Jolla Village Drive, MC 111-H, San Diego, CA 92161. Email: p1singh@health.ucsd.edu

outer medulla are metabolically active and rich in mitochondria. Particularly, proximal tubules are dependent on OXPHOS for ATP generation and use fatty acids, amino acids, and lactate to provide metabolites for the tricarboxylic acid (TCA) cycle within the mitochondria.[5] They have limited capacity to catabolize glucose as a metabolic fuel under physiological conditions. Other parts of the kidney, including thick ascending limb and glomerular and vascular cells, can effectively use glucose by *aerobic* glycolysis and inner medulla by *anaerobic* glycolysis. Nevertheless, overall energy generation in the kidney is largely provided by mitochondrial OXPHOS, except in the inner medulla.

Glucose oxidation by glycolysis generates pyruvate, which can be used as a substrate for mitochondrial OXPHOS under aerobic conditions, whereas in anaerobic conditions, pyruvate is converted to lactate. The preferential conversion of pyruvate to lactate even under aerobic conditions is referred to as the Warburg effect or aerobic glycolysis.[6,7] It has been described in cells undergoing proliferation under physiological and pathophysiological conditions. Glycolysis is inefficient in generating ATP, but it better supports macromolecular synthesis (nucleotides, amino acids) needed for cell regeneration.[6,7] Glycolytic metabolism plays an important role in nephron development. Nephron progenitors exhibit high rates of glycolysis to support cell proliferation and self-renewal.[8,9] After injury, recovery and repair of tubular cells also requires proliferation and redifferentiation, which may require metabolic adaptations, such as glycolysis. Whether a metabolic switch occurs in the kidney after injury to support proliferation and redifferentiation or how tubular metabolism evolves after injury in CKD is not well-understood. Hence, we conducted a detailed assessment of oxidative and glycolytic metabolism in the subtotal nephrectomy (STN) model of CKD in mice.

Methods

Experimental Animals

All experiments were conducted according to the NIH Guide for the Care and Use of Laboratory Animals and per the protocols approved by the Institutional Animal Care and Use Committee. All studies were performed in adult male 129 X1/Sv mice (Jackson Laboratories, Bar Habor, ME) at 9–12 weeks of age. Mice were fed regular chow and water and maintained under standard housing conditions.

Subtotal Nephrectomy Model of CKD

STN surgery was performed as described.[10] A small right flank incision (1 cm) was made. The muscles were clamped for 1 minute before cutting to prevent bleeding. The adrenal gland was then carefully separated from the right kidney. 3-0 silk ligature was tied around the right renal pedicle. The right pedicle was cut, and the right kidney was removed. The remaining fat, renal adrenal gland, and attached vascular tissues were returned to the retroperitoneum, and the incision was closed with silk suture for the muscle and then wound clips for the skin. Then, after a left flank incision, the left kidney retracted out of the peritoneal space to expose the renal artery. Two branches of the left renal artery were ligated with 3-0 silk suture. The kidney was gently placed back into the body, and the incision was closed as above. Wound clips were removed 14 days later. In sham groups, right and left flank incisions were made, and kidneys were exposed and briefly manipulated with cotton-tipped applicators and then returned to the abdomen. The incision was closed with silk suture for the muscle and wound clips for the skin.

GFR Measurement in Conscious Mice

GFR measurements were conducted by analyzing plasma kinetics of the GFR marker FITC-sinistrin (Fresenius-Kabi, Linz, Austria) after a bolus i.v. injection as previously described.[11] Briefly, FITC-Sinistrin (2% in 0.85% NaCl, which was also used to establish a standard curve) was injected into the retro-orbital plexus (2 μl/g body wt) during brief isoflurane anesthesia. At 3, 5, 7, 10, 15, 35, 56, and 75 minutes after injection, blood was collected from the tail vein into a Na^+-heparinized 10-μl microcap (Hirschmann Laborgeräte, Eberstadt, Germany). After centrifugation, plasma was diluted 1:10 in 0.5 mol/L HEPES (pH 7.4) and fluorescence determined with a Nanodrop ND-3300 fluorospectrometer (Thermo Scientific, Wilmington, DE) by pipetting 2 μl of samples onto the pedestal. GFR was calculated by a two-compartment model of two-phase exponential decay (GraphPad Prism, San Diego, CA). After baseline GFR measurements, mice underwent STN or sham surgery. Serial GFR measurements were performed in each mouse at 2, 4, 8, 12, and 16 weeks after sham and STN surgery.

Tail-Cuff BP Measurements in Conscious Mice

For serial BP measurements, the BP-2000 Blood Pressure Analysis System for mice from Visitech was used. Mice were placed and immobilized in mouse holders on a built-in heater plate that warms the animals for comfort (approximately 29°C) and increases blood flow to the tail. The tail-cuff and sensor system was put around the tail to determine BP as described.[12] Tails were passed through a cuff and immobilized by adhesive tape in a V-shaped block between a light source above and a photoresistor below the tail. Before recording BP measurements, mice were trained for approximately 7 days with the procedure for acclimatization. Evaluated photoelectrically, blood flow in the tails produces oscillating waveforms that were digitally sampled 200 times per second per channel. The waveforms are analyzed before and during a programmable routine of cuff inflation and deflation. After baseline measurements, mice underwent STN or sham surgery as described above. Serial BP measurements were performed in each mouse at 3, 7, 11, and 15 weeks after sham and STN surgery alternating with GFR measurements.

RNA Sequencing

Total RNA from sham and STN mice was extracted and isolated from homogenized mouse kidney tissues using a Qiagen RNeasy Plus Mini Kit (Qiagen, Hilden, Germany). Samples with compromised RNA integrity (RNA integrity number $\leq$8) were not included in the study. Samples meeting the RNA integrity criteria were used to generate RNA sequencing libraries, which were then multiplexed and single-end–sequenced with reads that were 50 base pairs in size. The sequencing depth was approximately

50 million reads per sample. The *Mus musculus* genome build GRCm38 was used as a reference to align the sequencing reads. Bowtie v1.3.0 was used for alignment, and RSEM v1.3.0 was used to perform read quantification and to generate the gene count matrix. Differential gene expression (DGE) analysis was performed using the EdgeR package. For the DGE analysis, genes with sufficient count (>100 cpm) in less than three samples were excluded. Log fold changes and *P* values comparing sham and STN were calculated for the remaining genes. Regulatory networks and canonical pathways were inferred from gene enrichment and biological pathway analysis using Ingenuity Pathway Analysis (2021; QIAGEN Redwood City). The Benjamini-Hochberg procedure was used to correct raw DGE *P* values to control for false discovery rate. Genes with corrected *P* values smaller than or equal to 0.05 were considered to be significantly under- or overexpressed. R v4.0.4 was used for data preprocessing, DGE analysis, and visualization.

Fresh Isolation of Renal Proximal Tubules

Mice were anesthetized with 100 mg/kg ketamine and 10 mg/kg xylazine by intraperitoneal injection, followed by cervical dislocation. As described previously,[13] kidneys were immediately removed and placed in a cold (0°C) Hanks Balanced Salt Solution (HBSS) (Invitrogen Corp., Carlsbad, CA). The renal capsule was removed, and the kidney was cut sagitally into two halves. The cortical tissue was removed, chopped/minced, and transferred to 10 ml of HBSS-containing Collagenase (Worthington Biochemical Corp., Lakewood, NJ) at 200 units/ml for digestion. Tubules were incubated at 37°C while rotating at 70 rpm for 15 minutes. The tubule suspension was mixed with a 10-ml pipet and returned to the incubator for an additional 15 minutes. After digestion, the tubules were divided into two 15-ml conical tubes with 5 ml per tube. Five milliliter of sterile, heat inactivated horse serum (Invitrogen Corp.) was added to each tube, and the tube was vortexed for 30 seconds. After one minute of sedimentation, the supernatant containing the proximal tubules was removed, transferred to another tube, and centrifuged for 7 minutes at 200 g. Tubules were washed once with 10 ml of HBSS and centrifuged at 200 g for 7 minutes. After 90%–95% of the supernatant was removed and discarded, tubules were resuspended in Renal Proximal Tubule Cells (RPTC) Media, which consisted of DMEM/F-12 culture media (Invitrogen Corp.) containing 15 mM of HEPES, 2.5 mM Glutamine, 1 μM Pyridoxine HCL, 15 mM Sodium Bicarbonate, 6 mM Sodium Lactate, 50 nM hydrocortisone, 50 μM L-ascorbic acid-2-phosphate, and Insulin-Transferrin-Selenium Solution (Invitrogen, 5, 2.75 mg/ml, and 3.35 ng/ml, respectively).

Ex Vivo Mitochondrial Oxygen Consumption

As described previously,[13–16] oxygen consumption in fresh, isolated proximal tubules was measured using an Agilent Seahorse XFe96 Extracellular Flux Analyzer. Tubules were seeded to a XF^e 96-well cell culture microplate in 180 μl of RPTC media. Isolated proximal tubules from sham and STN groups were examined simultaneously in the same microplate and analyzed accordingly. Oxygen consumption rate (OCR) was measured using mix/wait/measure times of 3/3/3 minutes. Sequential measurements were performed beginning with basal OCR; then after addition of the ATP synthase inhibitor, oligomycin (1 μM); followed by the pharmacological uncoupler, carbonyl cyanide p-trifluoro methoxyphenylhydrazone (FCCP) (0.5 μM); and finally with complex I (rotenone) and III (antimycin) inhibitors (0.5 μM) to each well per published protocols.[13–16] The key parameters measured included basal OCR, ATP-linked OCR, maximal OCR, spare or reserve capacity, and nonmitochondrial OCR. The decrease in OCR in response to oligomycin (ATP synthase inhibitor) reflects the ATP-linked OCR, and the remainder represents proton leak. The maximal OCR is the maximal rate of oxidation in the electron transport chain achieved with the dissipation of proton gradient by pharmacological uncouplers of OXPHOS, such as FCCP. The difference between the basal OCR and maximal OCR is referred to as the spare or reserve bioenergetic capacity. Nonmitochondrial OCR is the oxidation by nonmitochondrial enzymes, such as NADPH oxidases, lipoxygenases, and cyclooxygenases.

Ex Vivo Glycolysis Measurement

Glycolysis results in the extrusion of protons out of the cells, and this extracellular acidification rate (ECAR) was measured in fresh isolated proximal tubules using the Agilent Seahorse XF Glycolysis Stress Test kit as previously described.[13] Isolated proximal tubules from sham or STN mice were seeded to the XF^e 96-well cell culture microplate (Agilent Seahorse Bioscience) in 180 μl of RPTC media. Both groups were examined simultaneously in the same microplate and analyzed accordingly. Glucose, oligomycin, and 2-deoxyglucose (2-DG) were inserted through injection ports sequentially while measurements were made to calculate glycolytic capacity and reserve as described in the results section.

In separate experiments, we used the newer Seahorse XF Glycolytic Rate Assay, which determines the protons exported by cells into the assay medium over time, proton efflux rate (PER), expressed as pmol/min. Mitochondrial acidification is subtracted to determine glycolytic PER (glycoPER). The key parameter of this assay, glycoPER, correlates 1:1 with lactate accumulation over time. Isolated proximal tubules from sham or STN were seeded to the XFe 96-well cell culture microplate in 180 μl of Seahorse XF glycolytic rate assay media (containing glucose, glutamine, pyruvate, and HEPES buffer). Both groups were examined simultaneously in the same microplate and analyzed accordingly. Measurements were conducted under basal conditions and after mitochondrial electron transport chain inhibitor (rotenone and antimycin [0.5 μM]) injection and glycolysis inhibitor (2-DG [50 mM]) injection. The Agilent Seahorse glycolytic rate assay report generator was used to analyze and calculate basal and compensatory glycolysis, as described in the results section.

Western Blotting

Frozen kidneys were homogenized in a lysis buffer containing 20 mM Tris HCl (pH 7.5), 150 mM NaCl, 1 mM EGTA, 1% NP-40, 1% sodium deoxycholate, 2.5 mM sodium pyrophosphate, 1 mM β-glycerophosphate, 1 mM Na_3VO_4, and 1 μg/ml leupeptin, with

protease inhibitors (Roche) and phosphatase inhibitors (Cell Signaling). Protein concentration was determined using a DC protein assay (Bio-Rad). Protein lysates (50 μg of whole lysate) were separated by 4%–12% BisTris NuPAGE gels (Novex) in 1× MOPS SDS running buffer (Invitrogen). Proteins were transferred to the PVDF membrane (Invitrogen) in transfer buffer containing 1× transfer buffer (Invitrogen), 10% methanol, and 0.001% antioxidant (Invitrogen). The membranes were incubated in 5% milk and TBS-T blocking buffer for 1 hour in room temperature after which the immunoblots were incubated with the following primary antibodies overnight at 4°C: lactate dehydrogenase (LDH) A (Abcam, ab52488) and B (Abcam, ab85319); pyruvate dehydrogenase (PDH) E1 (Abcam, ab110334); pyruvate dehydrogenase kinases (PDK)1, 2, 3, and 4 (Abcam, ab110025, ab68164, ab182574, ab214938); and Viniculin (Millipore Sigma, V9264) used as a loading control. After removal of the primary antibodies, the immunoblots were incubated in secondary antibodies conjugated with HRP (Cell Signaling Technology) in room temperature for 1 hour. Completed immunoblots were imaged on the Chemidoc Imaging System (Bio-Rad Laboratories). Immunoblot images were analyzed with Image Lab Software (Bio-Rad, ver. 6.0.1).

Colorimetric Assays

Pyruvate (Cat. K354-100) and lactate (Cat. # K354-100) levels, hexokinases (HKs; Cat. # K354-100), phosphofructokinase (PFK; Cat. #K354-100), and LDH (Cat. # K354-100) activities were measured using Colorimetric Assay Kits from BioVision. Approximately 20 mg kidney tissue was homogenized in 200 μl assay buffer incubated for 20–60 minutes at room temperature, and the OD450nm was measured in a microplate reader (levels expressed as mU/ml).

Quantitative Real-Time RT-PCR

Kidneys were dissected and snap frozen in liquid nitrogen. Total RNA was prepared using the RNAeasy (Qiagen) method per the manufacturer's protocol. RNA concentrations were determined using a NanoDrop spectrophotometer, with an OD_{260}/OD_{280} ratio of >1.9 (indicating very high-quality RNA). cDNA was generated by RT-PCR using High-Capacity cDNA Reverse Transcription Kits (Applied Biosystems). Quantitative real-time RT-PCR was performed using the SYBR-green (Thermo Fisher Scientific) gene expression assay. Primer sequences are presented in Table 1.

Mitochondrial DNA Copy Measurement

Total DNA was isolated from the kidneys using the DNAeasy Blood and Tissue Kit (Qiagen, Valencia, CA) as described in the manufacturer's protocol. Extracted DNA was quantified, and 5 ng was used for PCR. Relative mitochondrial DNA content was assessed by quantitative real-time RT-PCR using primer for the mitochondrial-encoded *NADH dehydrogenase 1* (*NADH dehydrogenase subunit 1*) and was normalized to nuclear-encoded *β-actin*. Primer sequences for *NADH dehydrogenase subunit 1* and *β-actin* are presented in Table 1.

Statistical Methods

Results (other than transcriptomic analyses) were analyzed by the student *t* test. A *P* value of <0.05 was used to establish statistical significance. Unless stated otherwise, results are presented as group mean±SEM.

Results

Serial Renal Function Measurements after STN

We conducted *in vivo* experiments in STN or sham mice to assess GFR. Baseline GFR measurements with clearance of FITC-Sinistrin in conscious mice were conducted. After these measurements were made, mice were randomized to undergo STN or sham surgery. Serial GFR measurements in each mouse were conducted at 2, 4, 8, 12, and 16 weeks after sham and STN surgery. As shown in Figure 1A, GFRs in STN mice were significantly lower at each of these time points compared with baseline and with sham mice at the same time points. We also measured BP in mice at 3, 7, 11, and 15 weeks after STN or sham surgery (Figure 1B). Systolic

Table 1. Primer sequences for quantitative real-time RT-PCR and mitochondrial DNA copy measurement

Genes	Forward	Reverse
β-Actin	CACTGTCGAGTCGCGTCC	TCATCCATGGCGAACTGGTG
mtND-1	CTGTTCCGGGGAATGTGGAG	AGACAAGACTGATAGACGAGGGG
PGC1-α	AGACAGGTGCCTTCAGTTCAC	GCAGCACACTCTATGTCACTC
CPT1	GGTCTTCTCGGGTCGAAAGC	TCCTCCCACCAGTCACTCAC
CPT2	CAATGAGGAAACCCTGAGGA	GATCCTTCATCGGGAAGTCA
HK 1	CCAAAATAGACGAGGCCGTA	TTCAGCAGCTTGACCACATC
HK 2	TCAAAGAGAACAAGGGCGAG	AGGAAGCGGACATCACAATC
PFK	CCATGTTGTGGGTGTCTGAG	ACAGGCTGAGTCTGGAGCAT
PKM	CCATTCTCTACCGTCCTGTTG	TCCATGTAAGCGTTGTCCAG
LDHB	AGCATTCTGGGAAAGTCTCTGGCT	TGTCCACCACCATCTTATGCACCT
PDK 1	CACCACGCGGACAAAGG	GCCCAGCGTGACGTGAA
PDK 2	CCCCGTCCCCGTTGTC	TCGCAGGCATTGCTGGAT
PDK 3	GGAGCAATCCCAGCAGTGAA	TGATCTTGTCCTGTTTAGCCTTGT
PDK 4	CCATGAGAAGAGCCCAGAAGA	GAACTTTGACCAGCCTGTCTACAA

CPT, carnitine palmitoyltransferase; HK, hexokinase; PFK, phosphofructokinase; PKM, pyruvate kinase M; LDHB, lactate dehydrogenase B; PDK, pyruvate dehydrogenase kinase.

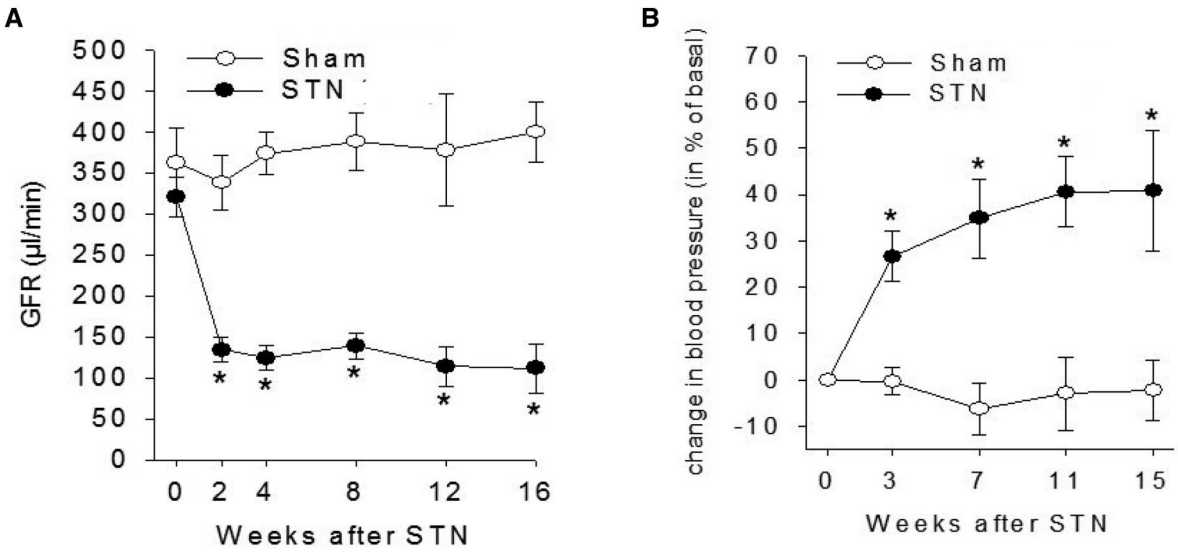

Figure 1. Renal function and BP changes after STN. (A) Serial assessment of GFR by FITC-sinistrin kinetics in conscious mice starting at baseline (time 0) and then at 2, 4, 8, 12, and 16 weeks after sham and STN surgery. (B) Serial tail-cuff BP measurements in conscious mice starting at baseline (time 0) and then at 3, 7, 11, and 15 weeks after sham and STN surgery alternating with GFR measurements. Data presented as mean±SEM. N=4 in sham and n=7 in STN. *$P < 0.05$ versus sham. STN, subtotal nephrectomy.

BP progressively increased in STN mice at each time point. On the basis of these results, we chose the 4-week time point for subsequent studies when GFRs were consistently reduced with modest BP elevation.

Enrichment of Metabolic Pathways on Transcriptomic Analyses in STN Kidneys

To gain a global perspective of the gene expression changes in renal metabolism, we conducted whole transcriptome sequencing in sham and STN kidneys at 4 weeks after surgery. DGE analysis was performed, and regulatory networks and canonical pathways were inferred from gene enrichment and biological pathway analysis using Ingenuity Pathway Analysis (2021; QIAGEN Redwood City). As shown in Figure 2A, the DGE profiles of sham and STN mice projected onto a multidimensional scaling plot show distinctive clustering between the groups. There was less homogeneity of DGE profiles within STN kidneys compared with sham.

A volcano plot of all differentially expressed genes with sufficient counts (>100 CPM) in more than two samples is shown in Figure 2B. In total, 1977 genes met the gene count threshold, and 872 genes were significantly differentially expressed after correction of the false discovery rate. Among the differentially expressed genes, 470 genes were overexpressed and 402 genes were underexpressed in STN kidneys compared with sham. Significant enrichment and differential regulation were observed in several biological pathways. The most over-represented biological group among these clusters was OXPHOS, which was surprisingly upregulated in STN compared with sham (Figure 2C). Targeted metabolic pathway analyses showed significant differential regulation of mitochondrial, fatty acid, and glucose metabolism pathways, and transcripts of several enzymes and transporters within these pathways were significantly altered (Table 2).

In the mitochondrial OXPHOS pathway, 48 genes were found to be differentially expressed between STN and sham kidneys (Figure 2, C and D). Several genes in this pathway were upregulated while genes encoding for TCA cycle enzymes and nicotinamide adenine dinucleotide biosynthesis were downregulated in STN kidneys. The expression of *uncoupling protein 2* was remarkably upregulated in the STN kidneys. Regarding fatty acid metabolism, few of the genes coding for enzymes of fatty acid beta oxidation and lipid biosynthesis pathways in mitochondria and peroxisomes were underexpressed (Figure 2C), whereas other genes were overexpressed in STN kidneys compared with sham (Figure 2D). Within the glycolytic and gluconeogenic pathways (Figure 2, C–E), most of the genes encoding for key enzymes were found to be overexpressed in the STN kidneys. In the PDH complex pathway, the expression of *pyruvate dehydrogenase E1 subunit α 1*, which catalyzes the conversion of pyruvate to acetyl CoA, was significantly reduced in STN kidneys (Figure 2, C–E). The expression of genes encoding PDK was not differentially regulated between STN and shams, whereas the expression of *pyruvate dehydrogenase phosphatase* (*Pdp*), which activates PDH from an inactive to active form, was significantly reduced in STN kidneys (Figure 2, C–E). In line with the changes in the metabolic pathways, the genes in the AMP kinase pathway were significantly underexpressed, suggesting impairment of energy regulation in the STN kidneys (Figure 2C). We also found overexpression of genes in the sirtuin and hypoxia inducible factor pathways in the STN kidney, suggesting increased transcriptional responses in the STN kidney (Figure 2C).

Metabolic Pathways Are Upregulated in STN Kidneys

To investigate tubular metabolism comprehensively in CKD, we examined the expression of key metabolic enzymes 4 weeks after STN. Carnitine palmitoyltransferase 1 and 2 (CPT1 and CPT2) are rate-limiting enzymes that

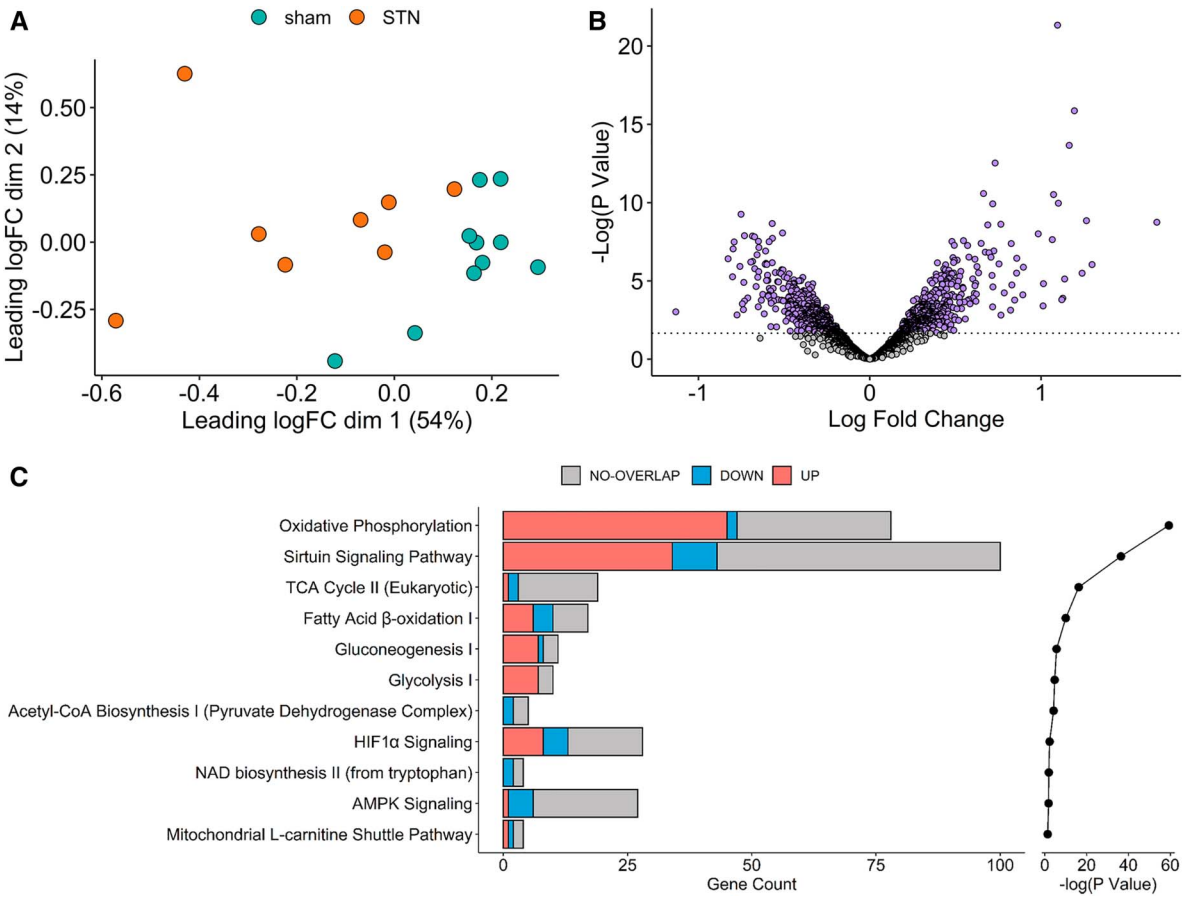

Figure 2. Transcriptomic analyses in STN kidneys. (A) DGE profiles in kidneys of sham and STN mice projected onto a MDS plot. Distinctive DGE profiles between sham and STN kidneys with less homogeneity of DGE profiles in STN compared with sham. *N*=10 in sham and 8 in STN. (B) Volcano plot of differentially expressed genes. Of the 1977 genes with sufficient counts (>100 CPM), 872 genes were significantly differentially expressed after correction of the false discovery rate, with 470 genes overexpressed and 402 genes underexpressed in STN kidneys compared with sham. (C) Predicted alternations in metabolic pathways. Several biological pathways were significantly enriched in STN kidneys, with oxidative phosphorylation being the most over-represented biological group. (D) Heat map of differentially regulated genes within metabolic pathways. Gene expression patterns were relatively consistent within the STN and sham groups, respectively, but distinctive when compared across the two groups. (E) Box plots of genes in the glycolytic and gluconeogenic pathways. Genes encoding for key enzymes HK1, PKM, GPI, ALDO A, PGAM1, and ENO1 overexpressed in the STN kidneys. Genes encoding for Pdha1 and Pdp underexpressed in STN kidneys. ALDO A, aldolase, fructose-bisphosphate A; DGE, differential gene expression; ENO1, enolase 1; GPI, glucose-6-phosphate isomerase; HK1, hexokinase; MDS, multidimensional scaling; Pdha1, pyruvate dehydrogenase E1 subunit α1; Pdp, pyruvate dehydrogenase phosphatase; PGAM1, phosphoglycerate mutase 1; PKM, pyruvate kinase M; STN, subtotal nephrectomy.

facilitate the transport of long-chain fatty acyl-CoAs into the mitochondria for fatty acid oxidation (FAO). We found increased mRNA levels of CPT1 and CPT2 in STN kidneys (Figure 3A). We also evaluated the expression and activities of various glycolytic enzymes in the STN kidneys (Figure 3, B and C). HKs catalyze the first step in the glycolytic pathway by converting glucose to glucose-6-phosphate and committing it to glycolysis. The transcriptional expression of *Hk1* and *Hk2* (Figure 3B) was significantly increased in STN kidneys. The mRNA levels of PFK, a rate-limiting enzyme that irreversibly converts fructose-6-phosphate to fructose-1, 6-bisphosphate, were significantly higher in STN compared with sham kidneys (Figure 3B). Pyruvate kinase (PK) is another rate-limiting glycolytic enzyme that catalyzes the final step in glycolysis by transferring a phosphoryl group from phosphoenolpyruvate to ADP to form pyruvate and ATP. There was a significant increase in mRNA levels of *Pkm* in STN kidneys (Figure 3B). The enzyme activities of both HK and PFK were also significantly increased in the STN kidneys (Figure 3C). These data suggest upregulation of both FAO and the glycolytic pathway in the STN kidneys.

Pyruvate Dehydrogenase Is Suppressed in STN Kidneys

The end product of glucose catabolism is pyruvate, which can be converted in the cytoplasm either to acetyl CoA or lactate. Acetyl CoA enters the TCA cycle in the mitochondria to power OXPHOS. Although we found higher expression and activities of glycolytic enzymes, the pyruvate content was reduced in STN kidneys (Figure 4A). We also found reduced lactate content in the STN kidneys (Figure 4B). The interconversion of and

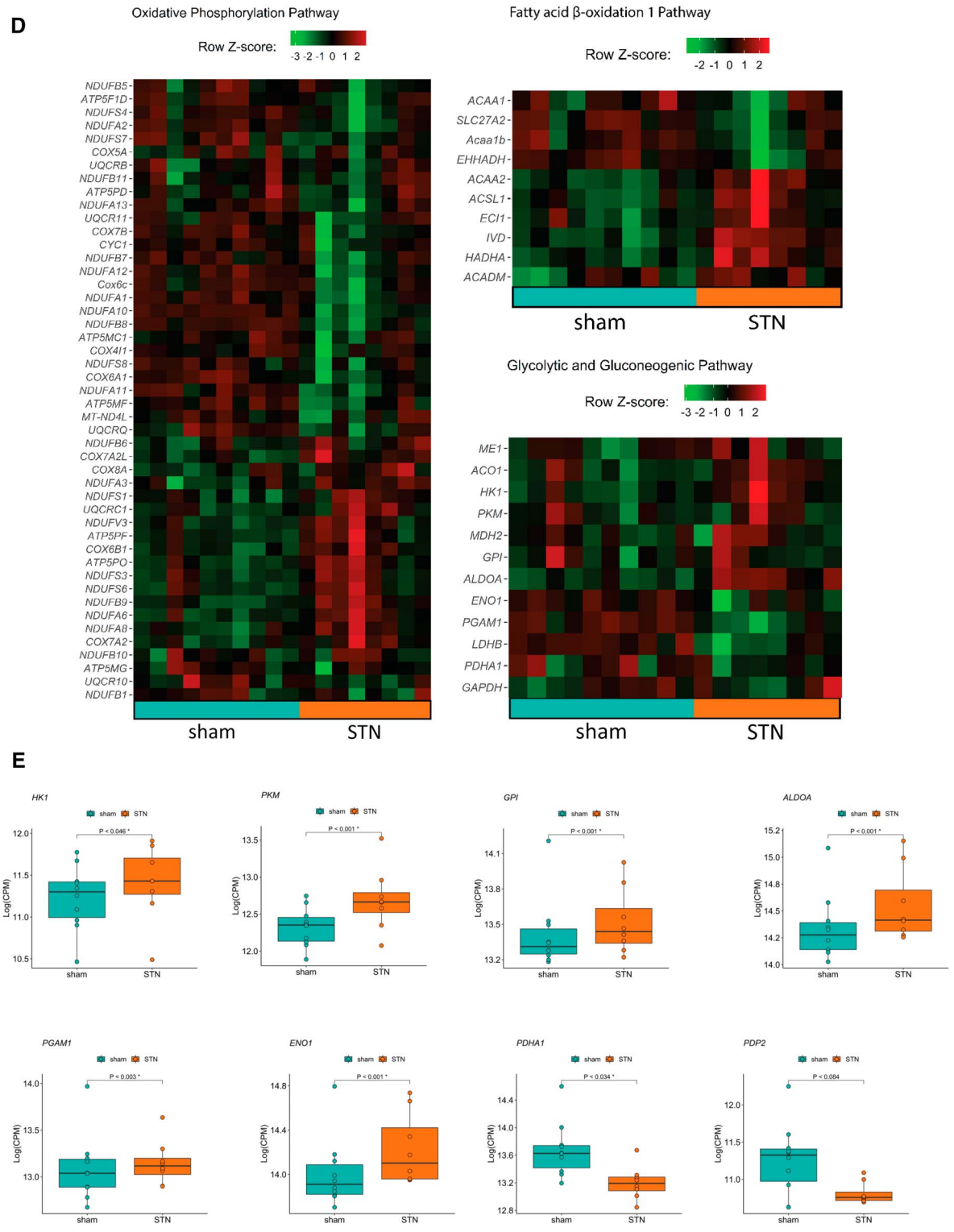

Figure 2. (Continued).

lactate is catalyzed by LDH, and its activity was significantly reduced in STN kidneys (Figure 4C). The protein expression of both LDH A and B subunits was reduced in the STN kidneys (Figure 4D). The conversion of pyruvate to acetyl CoA is catalyzed by PDH. There was no significant difference in PDH activity (*data not shown*), but the protein expression of the PDH E1 subunit was reduced in the STN kidneys (Figure 4E). There was a trend for reduced expression of pyruvate dehydrogenase phosphatase (PDP), which can dephosphorylate and activate PDH, in STN kidneys (*data not shown*). Phosphorylation (inactivation) of PDH is catalyzed by PDK. The protein expression

Table 2. RNA sequencing gene expression, log, and *P* value columns

Pathway Name	Z-Score	*P* Value	Gene Symbol	Gene Name
Oxidative phosphorylation	7.02	59.3	NDUFA12	NADH:ubiquinone oxidoreductase subunit A12
			COX6A1	Cytochrome c oxidase subunit 6A1
			NDUFV3	NADH:ubiquinone oxidoreductase subunit V3
			COX7B	Cytochrome c oxidase subunit 7B
			ATP5MC1	ATP synthase membrane subunit c locus 1
			Cox6c	Cytochrome c oxidase subunit 6C
			NDUFA6	NADH:ubiquinone oxidoreductase subunit A6
			ATP5PF	ATP synthase peripheral stalk subunit F6
			NDUFA3	NADH:ubiquinone oxidoreductase subunit A3
			ATP5PO	ATP synthase peripheral stalk subunit OSCP
			COX8A	Cytochrome c oxidase subunit 8A
			NDUFB10	NADH:ubiquinone oxidoreductase subunit B10
			ATP5MG	ATP synthase membrane subunit g
			UQCRQ	Ubiquinol-cytochrome *c* reductase complex III subunit VII
			UQCR11	Ubiquinol-cytochrome *c* reductase complex III subunit XI
			ATP5MF	ATP synthase membrane subunit f
			ATP5F1D	ATP synthase F1 subunit delta
			COX4I1	Cytochrome *c* oxidase subunit 4I1
			NDUFB9	NADH:ubiquinone oxidoreductase subunit B9
			UQCR10	Ubiquinol-cytochrome c reductase, complex III subunit X
			COX5A	Cytochrome c oxidase subunit 5A
			UQCRB	Ubiquinol-cytochrome c reductase binding protein
			NDUFA8	NADH:ubiquinone oxidoreductase subunit A8
			NDUFB7	NADH:ubiquinone oxidoreductase subunit B7
			NDUFA1	NADH:ubiquinone oxidoreductase subunit A1
			NDUFB1	NADH:ubiquinone oxidoreductase subunit B1
			COX7A2	Cytochrome c oxidase subunit 7A2
			COX7A2L	Cytochrome c oxidase subunit 7A2 like
			NDUFA2	NADH:ubiquinone oxidoreductase subunit A2
			NDUFA13	NADH:ubiquinone oxidoreductase subunit A13
			COX6B1	Cytochrome c oxidase subunit 6B1
			NDUFB11	NADH:ubiquinone oxidoreductase subunit B11
			CYC1	Cytochrome c1
			NDUFS6	NADH:ubiquinone oxidoreductase subunit S6
			ATP5PD	ATP synthase peripheral stalk subunit d
			NDUFS8	NADH:ubiquinone oxidoreductase core subunit S8
			NDUFS4	NADH:ubiquinone oxidoreductase subunit S4
			NDUFA11	NADH:ubiquinone oxidoreductase subunit A11
			NDUFB5	NADH:ubiquinone oxidoreductase subunit B5
			NDUFA10	NADH:ubiquinone oxidoreductase subunit A10
			MT-ND4L	NADH dehydrogenase, subunit 4L (complex I)
			NDUFS3	NADH:ubiquinone oxidoreductase core subunit S3
			NDUFB6	NADH:ubiquinone oxidoreductase subunit B6
			NDUFB8	NADH:ubiquinone oxidoreductase subunit B8
			NDUFS1	NADH:ubiquinone oxidoreductase core subunit S1
			UQCRC1	Ubiquinol-cytochrome c reductase core protein 1
			NDUFS7	NADH:ubiquinone oxidoreductase core subunit S7
TCA cycle II (Eukaryotic)	0.688	16.2	DHTKD1	Dehydrogenase E1 and transketolase domain containing 1
			MDH2	Malate dehydrogenase 2
			ACO1	Aconitase 1
Fatty acid b-oxidation I	0.728	9.98	ACAA2	Acetyl-CoA acyltransferase 2
			ECI1	Enoyl-CoA delta isomerase 1
			SLC27A2	Solute carrier family 27 member 2
			EHHADH	Enoyl-CoA hydratase and 3-hydroxyacyl CoA dehydrogenase
			ACSL1	Acyl-CoA synthetase long chain family member 1
			ACADM	Acyl-CoA dehydrogenase medium chain
			IVD	Isovaleryl-CoA dehydrogenase
			HADHA	Hydroxyacyl-CoA dehydrogenase trifunctional multienzyme complex subunit α
			Acaa1b	Acetyl-Coenzyme A acyltransferase 1B
			ACAA1	Acetyl-CoA acyltransferase 1

Table 2. (Continued).

Pathway Name	Z-Score	*P* Value	Gene Symbol	Gene Name
Gluconeogenesis I	2.714	5.58	ENO1	Enolase 1
			ALDOA	Aldolase, fructose-bisphosphate A
			GPI	Glucose-6-phosphate isomerase
			ENO1	Enolase 1
			MDH2	Malate dehydrogenase 2
			GAPDH	Glyceraldehyde-3-phosphate dehydrogenase
			ME1	Malic enzyme 1
			PGAM1	Phosphoglycerate mutase 1
Glycolysis I	3.162	4.68	ENO1	Enolase 1
			PKM	Pyruvate kinase M1/2
			ALDOA	Aldolase, fructose-bisphosphate A
			GPI	Glucose-6-phosphate isomerase
			ENO1	Enolase 1
			GAPDH	Glyceraldehyde-3-phosphate dehydrogenase
			PGAM1	Phosphoglycerate mutase 1
Acetyl-CoA biosynthesis I	−1.342	4.17	DBT	Dihydrolipoamide branched chain transacylase E2
			PDHA1	Pyruvate dehydrogenase E1 subunit α 1
HIF1a signaling	−0.192	2.28	MET	MET proto-oncogene, receptor tyrosine kinase
			PKM	Pyruvate kinase M1/2
			GPI	Glucose-6-phosphate isomerase
			MAP2K2	Mitogen-activated protein kinase kinase 2
			VEGFA	Vascular endothelial growth factor A
			HSPA8	Heat shock protein family A (Hsp70) member 8
			MAPK1	Mitogen-activated protein kinase 1
			LDHB	Lactate dehydrogenase B
			MTOR	Mechanistic target of rapamycin kinase
			HSP90AA1	Heat shock protein 90 α family class A member 1
			RPS6	Ribosomal protein S6
			RACK1	Receptor for activated C kinase 1
			HK1	Hexokinase 1
NAD biosynthesis II	−1	1.88	HAAO	3-Hydroxyanthranilate 3,4-dioxygenase
			AFMID	Arylformamidase
AMPK signaling	−0.655	1.8	AK4	Adenylate kinase 4
			SMARCA2	SWI/SNF-related, matrix-associated, actin-dependent regulator of chromatin, subfamily a, member 2
			PRKAA2	Protein kinase AMP-activated catalytic subunit α 2
			PTPA	Protein phosphatase 2 phosphatase activator
			MAPK1	Mitogen-activated protein kinase 1
			MTOR	Mechanistic target of rapamycin kinase
Mitochondrial L-carnitine shuttle	0	1.34	SLC27A2	Solute carrier family 27 member 2
			ACSL1	Acyl-CoA synthetase long chain family member 1

TCA, tricarboxylic acid.

of all four known isoforms of PDK—PDK1, 2, 3, and 4—was significantly reduced in STN kidneys (Figure 4F).

Alterations in Mitochondrial Biogenesis and Function in STN Kidneys

The high energy demands of the kidney are largely supported by mitochondrial OXPHOS. To further investigate changes in renal energy metabolism in the aftermath of injury, we conducted a detailed assessment of mitochondrial structural and functional integrity in the STN kidneys. We measured mitochondrial content and observed a significant increase in mitochondrial DNA copy number, a common biomarker to assess mitochondrial content, in the kidneys isolated from STN mice (Figure 5A). To assess mitochondrial biogenesis, we examined the expression of *peroxisome proliferator-activated receptor gamma coactivator 1-α* (Pgc-1α), which is a central regulator of mitochondrial biogenesis.[17] *Pgc-1α* mRNA expression was significantly increased in STN kidneys compared with controls (Figure 5A). This increase in mitochondrial content and biogenesis in the STN kidneys could indicate a compensatory response to injury. There were no consistent and significant differences in the expression of proteins that regulate mitochondrial dynamics, including Drp1, Fis1, Mfn 1&2, and Opa 1&2 (*data not shown*).

Proximal Tubular Mitochondrial Bioenergetics in STN Kidneys

Under physiological conditions, proximal tubules are dependent on OXPHOS for ATP generation and have limited capacity for glycolysis. Given the central role of proximal tubules in the development of fibrosis after

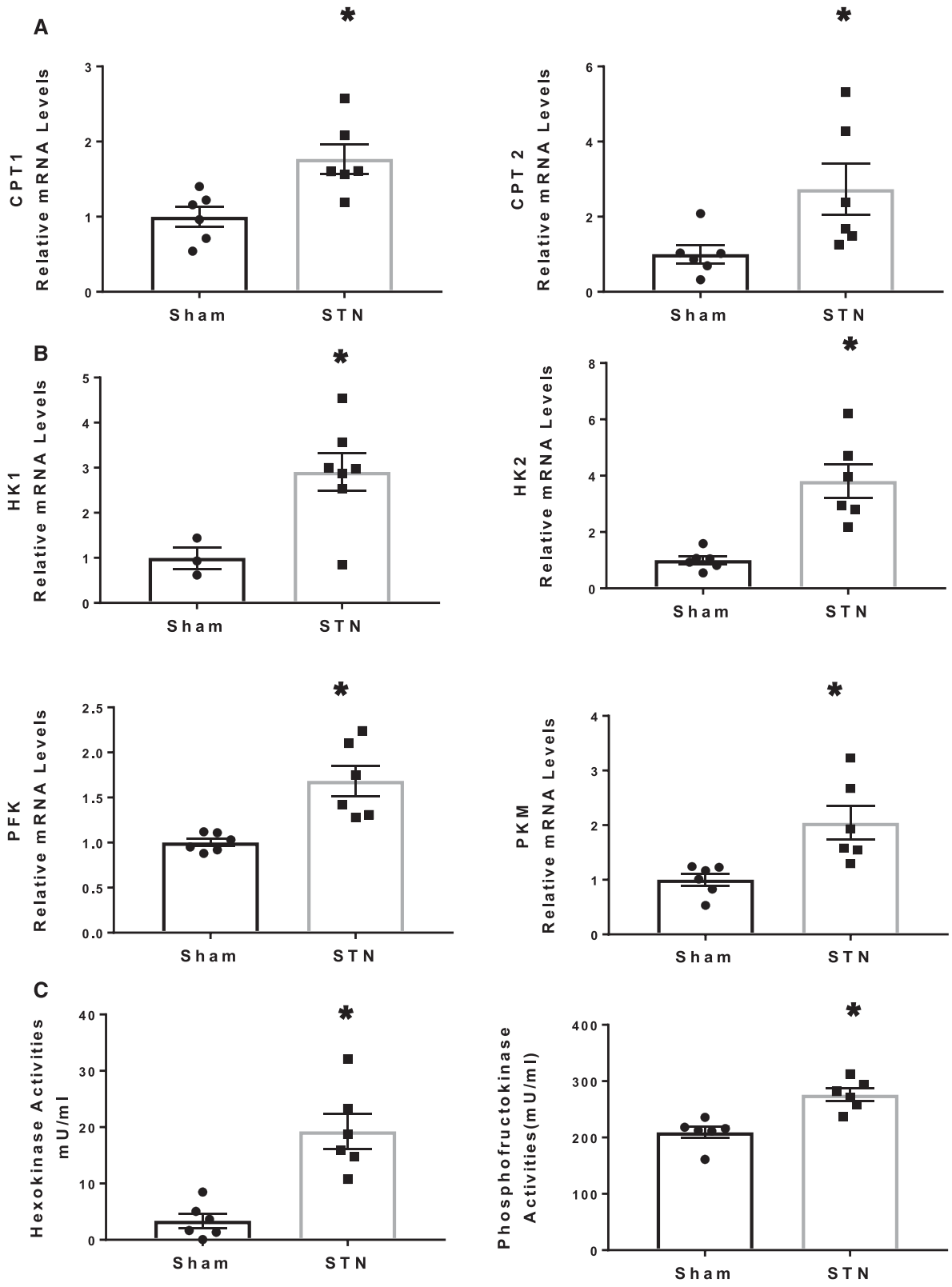

Figure 3. Increased metabolic pathways in STN kidneys. (A) Increased expression of fatty acid oxidation enzymes in STN kidneys. Real-time RT quantitative PCR with increased mRNA levels of CPT1 and CPT2 in STN kidneys. Data were presented as mean±SEM. $N=6$. *$P < 0.05$ versus sham. (B) Increased expression of glycolytic enzymes in STN kidneys. Real-time RT-quantitative PCR with increased mRNA levels of HK1 and HK2, PFK, and PKM in STN kidneys. Data were presented as mean±SEM. $N=6$. *$P < 0.05$ versus sham. (C) Increased activity of glycolytic enzymes in STN kidneys. Increased HK and PFK enzyme activities in STN kidneys by Colorimetric Assay. Data were presented as mean±SEM. $N=6$. *$P < 0.05$ versus sham. CPT, carnitine palmitoyltransferase; HK, hexokinases; PFK, phosphofructokinase; PKM, pyruvate kinase M; STN, subtotal nephrectomy.

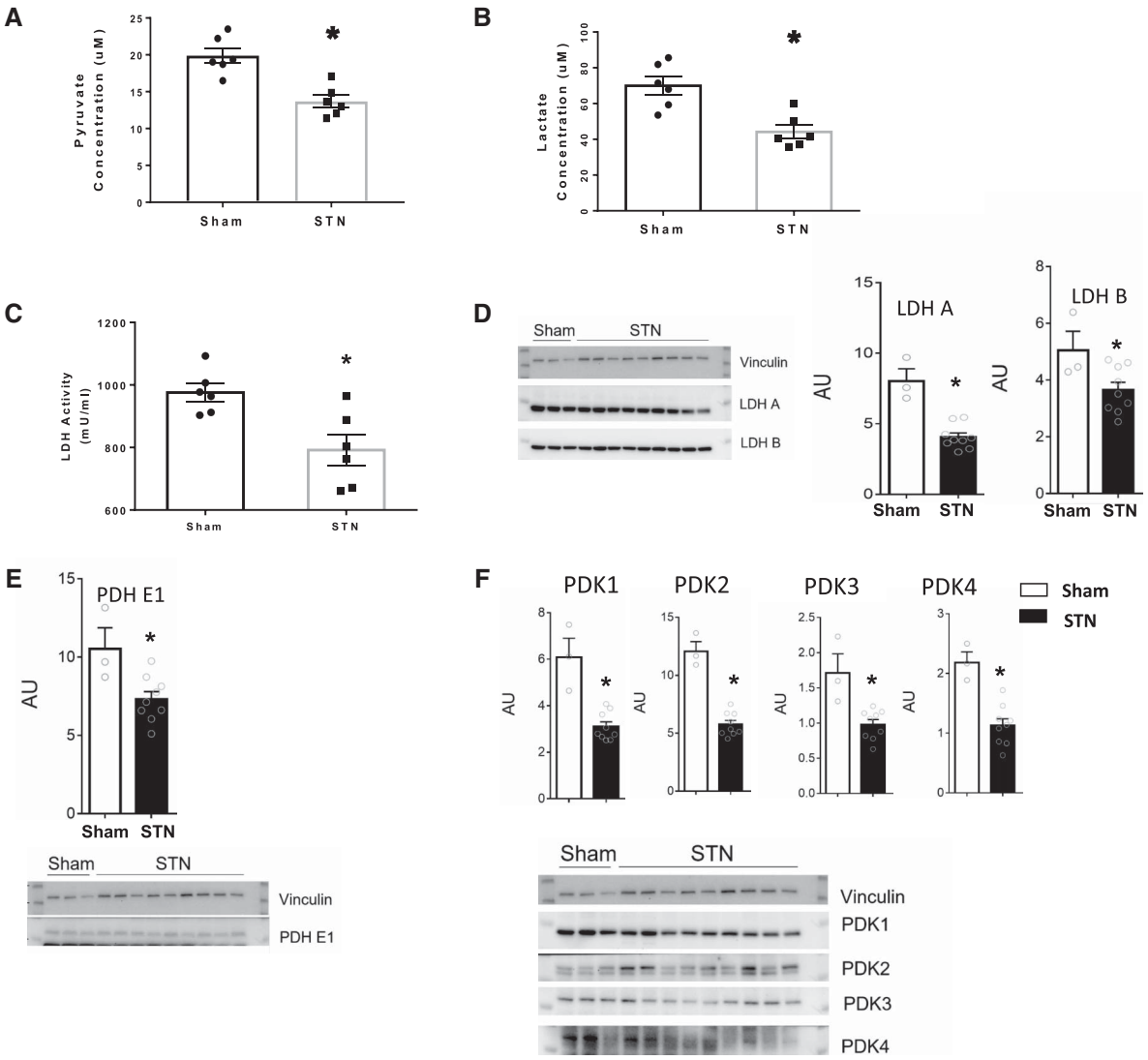

Figure 4. Regulation of pyruvate metabolism in STN kidneys. (A and B) Pyruvate and lactate concentrations, respectively, reduced in STN kidneys. (C and D) LDH activity and Western blot and densitometry showing protein expression of both LDH A and B subunits that were significantly reduced in the STN kidneys. (E) Western blot and densitometry showing protein expression of the PDH E1 subunit that was significantly reduced in the STN kidneys. (F) Western blot and densitometry showing protein expressions of PDK1, 2, 3, and 4 significantly reduced in STN kidneys. Data were presented as mean±SEM. N=3–6 in sham and 6 in STN. *$P < 0.05$ versus sham. LDH, lactate dehydrogenase; PDH, pyruvate dehydrogenase; PDK, pyruvate dehydrogenase kinases; STN, subtotal nephrectomy.

injury, we assessed fundamental parameters of mitochondrial bioenergetics in fresh isolated proximal tubules from sham and STN mice by examining mitochondrial OCRs as previously described.[13] As shown in Figure 5B, OCR at baseline was lower in STN proximal tubules compared with sham. Basal OCR, which is the minimum amount of mitochondrial OXPHOS needed to meet the energy demand, was significantly lower in proximal tubules isolated from STN kidneys compared with shams. We also observed significantly decreased ATP-linked OCR in tubules from STN kidneys, which indicates that the ATP synthesis in STN tubules may be compromised. The maximal OCR was substantially lower in STN tubules compared with control. Maximal OCR is a measure of the maximal rate of oxidation because of the dissipation of the proton gradient by pharmacological uncouplers of OXPHOS, such as FCCP, which increases proton permeability across the inner mitochondrial membrane. It reflects the maximum activity of electron transport and substrate oxidation achievable by cells.[15,16] The difference between the basal OCR and maximal OCR is referred to as the spare or reserve bioenergetic capacity, which was not different between STN and sham tubules. It estimates the maximal capacity for OXPHOS with increased ATP demand or in response to acute stress.[15,16] Additional parameters of mitochondrial bioenergetics that are internally normalized include respiratory control ratio (RCR), which is the ratio of the FCCP-induced maximal OCR to proton leak.[15,16] High RCR implies that the mitochondria has a high capacity for substrate oxidation and a low proton leak. RCR was significantly lower in STN tubules (Figure 5C). Coupling

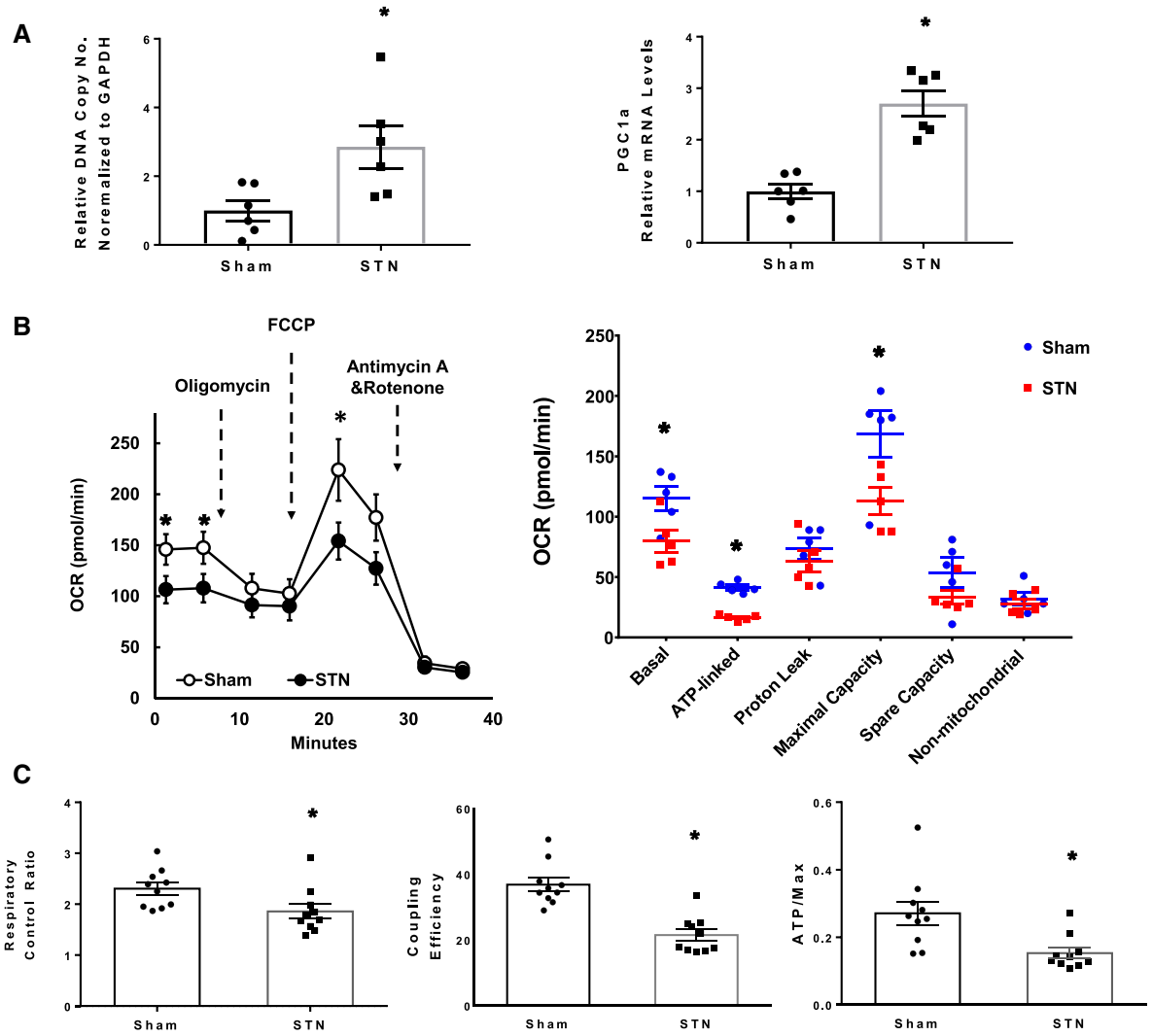

Figure 5. Mitochondrial function in STN kidneys. (A) Mitochondrial content and biogenesis. Relative mitochondrial DNA copy number and mRNA levels of PGC1-α by real-time RT-quantitative PCR increased in the STN kidneys. Data were presented as mean±SEM. N=6. *$P < 0.05$ versus sham. (B) Proximal tubular mitochondrial bioenergetics. Mitochondrial respiration in fresh isolated tubules from sham and STN kidneys analyzed by measuring OCR using the Agilent Seahorse XFe96 extracellular flux analyzer and Cell Mito Stress Test Kit. OCR was measured under basal conditions, followed by the sequential addition of oligomycin (0.5 μM), FCCP (4 μM), rotenone (1 μM), or antimycin A (1 μM). Each data point represents an OCR measurement. Individual parameters for basal, ATP-linked, proton leak, maximal capacity, spare capacity, and nonmitochondrial respiration in fresh isolated tubules from each group. Basal, ATL-linked, and maximal OCRs were significantly lower in STN tubules. (C) Proximal tubular mitochondrial efficiency. RCR, coupling efficiency, and ATP/Max OCR were all significantly lower in STN tubules. Data were presented as mean±SEM. N=5. *$P < 0.05$ versus sham. FCCP, carbonyl cyanide p-trifluoro methoxyphenylhydrazone; OCR, oxygen consumption rate; RCR, respiratory control ratio; STN, subtotal nephrectomy.

efficiency is the proportion of basal OCR used for ATP synthesis and is determined by the change in basal respiration rate with the addition of oligomycin.[15,16] It is calculated by the ratio of ATP-linked OCR to basal OCR. Coupling efficiency was reduced significantly in STN kidneys (Figure 5C). Finally, the ratio of ATP-linked respiration to maximal respiration can estimate how closely OXPHOS is making ATP relative to its maximal capacity.[15,16] This was also decreased significantly in STN (Figure 5C). These results suggest that several parameters of mitochondrial function are impaired in STN tubules, despite an upregulation of metabolic pathways.

Proximal Tubular Glycolysis Is Upregulated in STN Kidneys

We examined functional glycolysis in fresh isolated proximal tubules from sham and STN kidneys using Agilent Seahorse XF glycolytic assays. During glycolysis, the conversion of glucose to pyruvate, and subsequently lactate, results in a net production and extrusion of protons into the extracellular medium, resulting in the acidification of the medium surrounding the cell. The acidification of the medium was directly measured and reported as ECAR using the Agilent Seahorse XF Glycolysis Stress Test kit.[13,18] ECAR was measured at the basal condition, followed by sequential administration of glucose, oligomycin, and 2-DG. Glucose is supplied to feed glycolysis, and the

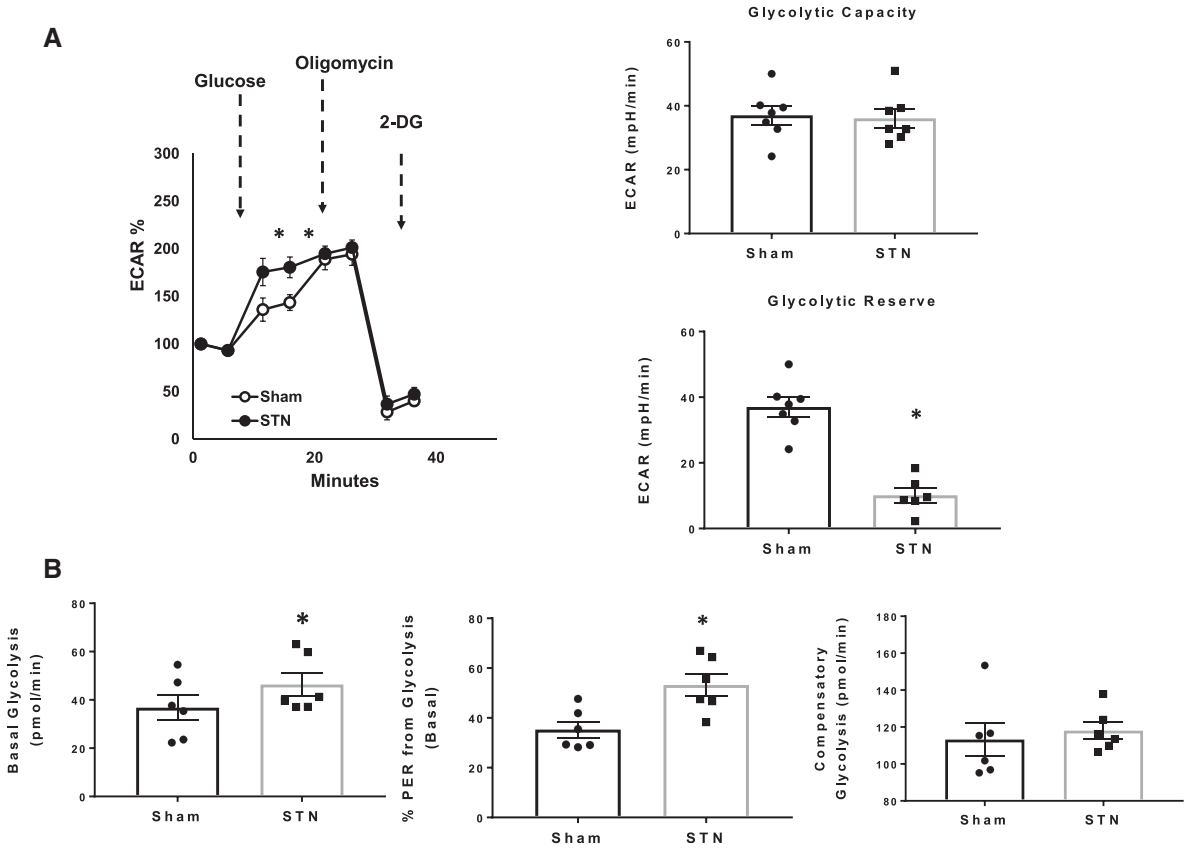

Figure 6. Functional glycolysis in STN kidneys. (A) Proximal tubular glycolysis in fresh isolated tubules from sham and STN kidneys measured by ECAR in response to sequential compound injections of glucose (10 mM), oligomycin (1 μM), and 2-deoxyglucose (2DG; 50 mM) using the Agilent Seahorse XFe96 extracellular flux analyzer and Agilent Seahorse XF Glycolysis Stress Test kit. Increased ECAR, similar glycolytic capacity, and lower glycolytic reserve observed in STN tubules. Data presented as mean±SEM, N=7. *$P < 0.05$ versus sham. (B) Proximal tubular glycolysis measured by proton efflux rate (PER) in fresh isolated tubules from sham and STN kidneys using the Agilent Seahorse XFe96 extracellular flux analyzer and Agilent Seahorse XF Glycolytic Rate Assay Kit. Basal PER and percent PER from glycolysis increased in STN tubules. Data presented as mean±SEM, N=6. *$P < 0.05$ versus sham. ECAR, extracellular acidification rate; STN, subtotal nephrectomy.

difference of ECAR before and after the addition of glucose indicates the basal rate of glycolysis. The glycolytic rate induced by addition of glucose as a percentage of baseline was significantly higher in STN tubules (Figure 6A). Oligomycin stops OXPHOS by inhibiting ATP synthase. Maximum ECAR after the addition of oligomycin reflects the glycolytic capacity of cells. The glycolytic capacity was similar in tubules from sham and STN kidneys (Figure 6A). The difference between glycolytic capacity and the basal glycolysis rate is the glycolytic reserve of the cells, which reflects the ability to respond to an energetic demand. We observed a significantly lower glycolytic reserve in STN tubules (Figure 6A), which could reflect depleted glycolytic response due to increased basal glycolysis.

Pyruvate, obtained from the catabolism of glucose, can either be converted to lactate in the cytoplasm or enter the TCA cycle in the mitochondria, and both processes release protons leading to extracellular acidification. To further confirm our results, we performed additional measurements with the Agilent Seahorse XF Glycolytic Rate Assay.[13] It provides more specific measurement for glycolytic acidification by simultaneously measuring mitochondrial and glycolytic proton efflux rates (PER) to calculate glycoPER, by subtracting the mitochondrial CO_2–derived PER from the total PER. GlycoPER is also referred to as basal glycolysis. The mitochondrial electron chain inhibitors rotenone and antimycin A (Rot/AA) induce a switch to glycolysis in the cells to meet the energy demands. Upregulated PER in response to rotenone and antimycin A is referred to as compensatory glycolysis. Basal PER was increased in STN tubules compared with sham (Figure 6B). Given that mitochondrial OCR was lower in STN, this likely reflects the PER from glycolysis. This was confirmed by increased percent PER from glycolysis (Figure 6B), which indicates the amount of acidification due to glycolysis versus other sources, such as mitochondrial CO_2. Compensatory glycolysis was not different between the groups. These data indicate increased functional glycolysis in tubular cells in STN.

Discussion

There has been a long-standing interest in renal metabolism, and lately, increasing evidence points to its important role in the pathophysiology of kidney disease. An increase in metabolic flux in glycolysis, FAO, and TCA cycle has been described in the kidney cortex of db/db type

2 diabetic mice.[19] Similar findings of enrichment of various metabolic pathways have been found in kidney biopsy samples of patients with diabetes.[19] Interestingly, despite evidence of increased metabolic flux, there was clear evidence for mitochondrial dysfunction with increased proton leak, diminished ATP production, and decreased expression of electron transport chain complexes.

We also observed similar findings of significant enrichment of metabolic pathways in the STN kidney by transcriptomic analyses. Several genes in the mitochondrial OXPHOS pathway and FAO pathway were overexpressed in STN kidneys while others were downregulated. Most genes in the glycolytic and gluconeogenic pathways were upregulated. There was increased expression of rate-limiting FAO and glycolytic enzymes in the STN kidney, suggesting increased metabolic flux similar to the findings discussed above in diabetic kidneys. Notably, despite an increase in the expression of rate-limiting metabolic enzymes to provide substrates for mitochondrial metabolism, functional assessment of the mitochondria revealed suppressed OXPHOS in proximal tubules in the STN kidneys. Importantly, bioenergetic parameters revealed low RCR, which indicates lower capacity for substrate oxidation by the mitochondria. Coupling efficiency, which is the proportion of mitochondrial respiration used for ATP synthesis, was also reduced. These findings provide evidence for primary mitochondrial dysfunction, likely due to impaired substrate utilization and ATP synthesis, and explain the suppressed mitochondrial OXPHOS despite increased metabolic pathways. Other parameters of mitochondrial content and morphology were not impaired and mitochondrial biogenesis/content was increased, likely as a compensatory response to mitochondrial dysfunction. Because one of the major determinants of mitochondrial respiration is ATP demand, another possibility to consider is that the reduced OXPHOS may be in response to low ATP demand in the STN kidney because of reduced GFR and filtered load for reabsorption. However, the observed decrease in RCR and coupling efficiency point toward primary mitochondrial dysfunction, which needs to be further characterized. Finally, the discrepancy may be from transcriptomic analyses conducted in whole kidneys while functional mitochondrial studies were performed in isolated tubules. However, given that most metabolic activity in the kidneys occurs in the kidney cortex largely composed proximal tubules, this seems less likely.

In mouse models of advanced fibrosis, lowered levels of enzymes and regulators involved in FAO have been observed.[20] This discrepancy may reflect temporal changes with metabolic adaptations in the earlier stages of CKD versus advanced fibrosis in late stages. A direct role of impaired FAO in the development of fibrosis has been shown where overexpression of CPT1A in renal tubules was protective in reducing fibrosis.[21] Changes in gene expression of FAO and OXPHOS pathways have also been observed in n patients with CKD.[22]

Altered glucose metabolism with upregulation of rate-limiting glycolytic enzymes and reduced FAO enzymes has been observed in animal models of polycystic kidney disease, and pharmacological targeting of glycolysis by inhibition with 2-deoxyglucose decreased cystogenesis.[23–25] However, in other models of advanced CKD, folic acid nephropathy,[21] and aristolochic acid,[26] there was a general downregulation of genes in the glycolytic pathway. There is evidence, although limited, for activation of glycolysis in other models of CKD. Increased glycolytic enzyme mRNA expression was observed in UUO kidneys[27] and atrophied, postischemic kidney tubules with surrounding fibrosis.[28] Our novel investigations are among the first to directly assess functional glycolysis and demonstrate increased glycolysis in proximal tubular cells in STN kidneys. Moreover, our approach provides greater relevance to *in vivo* conditions by making these measurements in functional, intact cells with a preserved cellular environment and interactions of the mitochondria with other cellular organelles.

The PDH-PDK axis is the key regulatory point of metabolic reprogramming between OXPHOS and glycolysis. PDH converts pyruvate to acetyl CoA, committing it to OXPHOS. PDK inhibits PDH by phosphorylation and curbs the pyruvate entry into OXPHOS.[29] Thus, the PDH-PDK axis serves as a gatekeeper for energy metabolism. There is accumulating evidence on the importance of the PDH-PDK pathway in the pathogenesis of diabetes, heart failure, and cancer.[29] We observed a significant decrease in the expression of enzymes involved in pyruvate metabolism, suggesting decreased conversion of pyruvate to acetyl CoA to feed the TCA cycle and mitochondrial OXPHOS. This could also play a role in the suppressed mitochondrial OXPHOS due to limited substrate availability to generate reducing equivalents for the electron transport chain. We also observed decreased pyruvate and lactate levels. Possible explanations include shunting of early glycolytic intermediates to the pentose phosphate pathway, which is active in proliferating cells.[5,8] It can be hypothesized that in response to injury, glycolysis may be activated in STN kidneys not necessarily for energy generation by intermediates for the TCA cycle, but to provide carbon intermediates for proliferation of cells as a repair mechanism. Alternatively, there should be shunting of pyruvate and lactate to gluconeogenesis by the tubular cells, supported by our findings of upregulation of the genes coding for several key gluconeogenic enzymes in the STN kidneys.

In conclusion, we have provided a detailed assessment of mitochondrial function and metabolic changes in the CKD kidney. There is significant enrichment in metabolic pathways per transcriptomic analyses in the STN kidneys. Yet, proximal tubular mitochondrial respiration and function is suppressed likely because of primary mitochondrial dysfunction in substrate utilization and ATP synthesis. Further studies are warranted to unravel underlying mechanisms for these findings, and we are actively pursuing them. There is proximal tubular metabolic reprogramming toward glycolysis, which, whether adaptive to enhance repair or maladaptive leading to fibrosis, could be an important therapeutic target to alter the course of CKD and needs to be studied further.

Disclosures

Y. Li reports the following: Advisory or Leadership Role: Boren Pharm; Employer: Boren Pharm, Explora Biolabs—a Charles River Company; and Ownership Interest: Boren Pharm. P. Singh reports the following: Advisory or Leadership Role: *American Journal of Physiology*: Renal Editorial Board; ASN *Kidney360*: Associate Editor; Consultancy: Vividion Therapeutics; NIH PBKD: Permanent

Member; Other Interests or Relationships: American Society of Nephrology; American Physiological Society; and Research Funding: Bristol Myers Squibb. All remaining authors have nothing to disclose.

Funding

This work was supported by VA Merit BX002175 (PS), NIH R01 DK107852 (PS), VA CDA2 IK2BX004338-01 (MH), NIH R01-HL145470 (TSS), and resources from the UAB-UCSD O'Brien Center (NIH P30-DK 079337).

Acknowledgments

Some of the results have been presented as abstracts at American Society of Nephrology and Experimental Biology Meetings.

Author Contributions

Conceptualization: Prabhleen Singh.
Data curation: Wanjun Gu, Mark Hepokoski, Young Chul Kim, Ying Li, Hai Pham, Prabhleen Singh, Rick Tham.
Formal analysis: Wanjun Gu, Young Chul Kim, Ying Li, Hai Pham, Tatum S. Simonson, Rick Tham.
Funding acquisition: Prabhleen Singh.
Investigation: Wanjun Gu, Young Chul Kim, Ying Li, Hai Pham, Tatum S. Simonson, Rick Tham.
Methodology: Wanjun Gu, Mark Hepokoski, Young Chul Kim, Ying Li, Hai Pham, Tatum S. Simonson, Rick Tham.
Project administration: Prabhleen Singh.
Resources: Prabhleen Singh.
Supervision: Mark Hepokoski, Tatum S. Simonson, Prabhleen Singh.
Validation: Wanjun Gu, Ying Li, Tatum S. Simonson, Prabhleen Singh.
Writing – original draft: Ying Li.
Writing – review and editing: Wanjun Gu, Mark Hepokoski, Ying Li, Tatum S. Simonson, Prabhleen Singh.

References

1. Centers for Disease Control and Provention. *Chronic Kidney Disease in the United States, 2021*. https://www.cdc.gov/kidneydisease/publications-resources/CKD-national-facts.html. Accessed August 2022
2. Grgic I, Campanholle G, Bijol V, et al. Targeted proximal tubule injury triggers interstitial fibrosis and glomerulosclerosis. *Kidney Int.* 2012;82(2):172–183. doi:10.1038/ki.2012.20
3. Takaori K, Nakamura J, Yamamoto S, et al. Severity and frequency of proximal tubule injury determines renal prognosis. *J Am Soc Nephrol.* 2016;27(8):2393–2406. doi:10.1681/ASN.2015060647
4. Mandel LJ. Primary active sodium transport, oxygen consumption, and ATP: coupling and regulation. *Kidney Int.* 1986;29(1):3–9. doi:10.1038/ki.1986.2
5. Singh P, Thomson SC, McDonough AA. Metabolic basis of solute transport. In: *Brenner and Rector's the Kidney*, 11th ed. Elsevier; 2019.
6. Vander Heiden MG, Cantley LC, Thompson CB. Understanding the Warburg effect: the metabolic requirements of cell proliferation. *Science.* 2009;324(5930):1029–1033. doi:10.1126/science.1160809
7. Lunt SY, Vander Heiden MG. Aerobic glycolysis: meeting the metabolic requirements of cell proliferation. *Annu Rev Cell Dev Biol.* 2011;27(1):441–464. doi:10.1146/annurev-cellbio-092910-154237
8. Cargill K, Sims-Lucas S. Metabolic requirements of the nephron. *Pediatr Nephrol.* 2020;35(1):1–8. doi:10.1007/s00467-018-4157-2
9. Liu J, Edgington-Giordano F, Dugas C, et al. Regulation of nephron progenitor cell self-renewal by intermediary metabolism. *J Am Soc Nephrol.* 2017;28(11):3323–3335. doi:10.1681/ASN.2016111246
10. Ma LJ, Fogo AB. Model of robust induction of glomerulosclerosis in mice: importance of genetic background. *Kidney Int.* 2003;64(1):350–355. doi:10.1046/j.1523-1755.2003.00058.x
11. Qi Z, Whitt I, Mehta A, et al. Serial determination of glomerular filtration rate in conscious mice using FITC-inulin clearance. *Am J Physiol Renal Physiol.* 2004;286(3):F590–F596. doi:10.1152/ajprenal.00324.2003
12. Krege JH, Hodgin JB, Hagaman JR, Smithies O. A noninvasive computerized tail-cuff system for measuring blood pressure in mice. *Hypertension.* 1995;25(5):1111–1115. doi:10.1161/01.hyp.25.5.1111
13. Li Y, Nourbakhsh N, Pham H, Tham R, Zuckerman JE, Singh P. Evolution of altered tubular metabolism and mitochondrial function in sepsis-associated acute kidney injury. *Am J Physiol Renal Physiol.* 2020;319(2):F229–F244. doi:10.1152/ajprenal.00390.2019
14. Beeson CC, Beeson GC, Schnellmann RG. A high-throughput respirometric assay for mitochondrial biogenesis and toxicity. *Anal Biochem.* 2010;404(1):75–81. doi:10.1016/j.ab.2010.04.040
15. Brand MD, Nicholls DG. Assessing mitochondrial dysfunction in cells. *Biochem J.* 2011;435(2):297–312. doi:10.1042/bj20110162
16. Divakaruni AS, Paradyse A, Ferrick DA, Murphy AN, Jastroch M. Analysis and interpretation of microplate-based oxygen consumption and pH data. *Methods Enzymol.* 2014;547:309–354. doi:10.1016/B978-0-12-801415-8.00016-3
17. Weinberg JM. Mitochondrial biogenesis in kidney disease. *J Am Soc Nephrol.* 2011;22(3):431–436. doi:10.1681/ASN.2010060643
18. Gerriets VA, Kishton RJ, Nichols AG, et al. Metabolic programming and PDHK1 control CD4+ T cell subsets and inflammation. *J Clin Invest.* 2015;125(1):194–207. doi:10.1172/jci76012
19. Sas KM, Kayampilly P, Byun J, et al. Tissue-specific metabolic reprogramming drives nutrient flux in diabetic complications. *JCI Insight.* 2016;1(15):e86976. doi:10.1172/jci.insight.86976
20. Kang HM, Ahn SH, Choi P, et al. Defective fatty acid oxidation in renal tubular epithelial cells has a key role in kidney fibrosis development. *Nat Med.* 2015;21(1):37–46. doi:10.1038/nm.3762
21. Miguel V, Tituana J, Herrero JI, et al. Renal tubule Cpt1a overexpression protects from kidney fibrosis by restoring mitochondrial homeostasis. *J Clin Invest.* 2021;131(5):e140695. doi:10.1172/jci140695
22. Granata S, Zaza G, Simone S, et al. Mitochondrial dysregulation and oxidative stress in patients with chronic kidney disease. *BMC Genomics.* 2009;10(1):388. doi:10.1186/1471-2164-10-388
23. Chiaravalli M, Rowe I, Mannella V, et al. 2-Deoxy-d-Glucose ameliorates PKD progression. *J Am Soc Nephrol.* 2016;27(7):1958–1969. doi:10.1681/ASN.2015030231
24. Nowak KL, Hopp K. Metabolic reprogramming in autosomal dominant polycystic kidney disease: evidence and therapeutic potential. *Clin J Am Soc Nephrol.* 2020;15(4):577–584. doi:10.2215/CJN.13291019
25. Rowe I, Chiaravalli M, Mannella V, et al. Defective glucose metabolism in polycystic kidney disease identifies a new therapeutic strategy. *Nat Med.* 2013;19(4):488–493. doi:10.1038/nm.3092
26. Harzandi A, Lee S, Bidkhori G, et al. Acute kidney injury leading to CKD is associated with a persistence of metabolic dysfunction and hypertriglyceridemia. *iScience.* 2021;24(2):102046. doi:10.1016/j.isci.2021.102046
27. Ding H, Jiang L, Xu J, et al. Inhibiting aerobic glycolysis suppresses renal interstitial fibroblast activation and renal fibrosis. *Am J Physiol Renal Physiol.* 2017;313(3):F561–F575. doi:10.1152/ajprenal.00036.2017
28. Lan R, Geng H, Singha PK, et al. Mitochondrial pathology and glycolytic shift during proximal tubule atrophy after ischemic AKI. *J Am Soc Nephrol.* 2016;27(11):3356–3367. doi:10.1681/ASN.2015020177
29. Stacpoole PW. Therapeutic targeting of the pyruvate dehydrogenase complex/pyruvate dehydrogenase kinase (PDC/PDK) axis in cancer. *J Natl Cancer Inst.* 2017;109(11):1–14. doi:10.1093/jnci/djx071

Received: September 1, 2022 **Accepted:** May 8, 2023
Published Online Ahead of Print: May 24, 2023

Y. Li and W. Gu are co-first authors.

See related editoiral, "Energy Metabolism in CKD: Running Low on Fuel" on pages 1014–1016.